

Role of radially aligned scleral collagen fibers in optic nerve head biomechanics

Yi Hua^a, Andrew P. Voorhees^a, Ning-Jiun Jan^{a,b}, Bingrui Wang^{a,d}, Susannah Waxman^a, Joel S. Schuman^{e,f,g,h}, Ian A. Sigal^{a,b,c,*}

^a Department of Ophthalmology, University of Pittsburgh, Pittsburgh, PA, USA

^b Department of Bioengineering, University of Pittsburgh, Pittsburgh, PA, USA

^c McGowan Institute for Regenerative Medicine, University of Pittsburgh School of Medicine, University of Pittsburgh, Pittsburgh, PA, USA

^d School of Mechanical Engineering, Southwest Jiaotong University, Chengdu, Sichuan, China

^e Department of Ophthalmology, NYU Langone Health, NYU Grossman School of Medicine, New York, NY, USA

^f Center for Neural Science, NYU, New York, NY, USA

^g Department of Biomedical Engineering, NYU Tandon School of Engineering, Brooklyn, NY, USA

^h Department of Physiology and Neuroscience, Neuroscience Institute, NYU Langone Health, NYU Grossman School of Medicine, New York, NY, USA

ARTICLE INFO

Keywords:

Collagen
Sclera
Optic nerve head
Microstructure
Biomechanics

ABSTRACT

Collagen fibers organized circumferentially around the canal in the peripapillary sclera are thought to provide biomechanical support to the sensitive tissues within the optic nerve head (ONH). Recent studies have demonstrated the existence of a family of fibers in the innermost sclera organized radially from the scleral canal. Our goal was to determine the role of these radial fibers in the sensitivity of scleral canal biomechanics to acute increases in intraocular pressure (IOP). Following the same general approach of previous parametric sensitivity studies, we created nonlinear generic finite element models of a posterior pole with various combinations of radial and circumferential fibers at an IOP of 0 mmHg. We then simulated the effects of normal and elevated IOP levels (15 and 30 mmHg). We monitored four IOP-induced geometric changes: peripapillary sclera stretch, scleral canal displacement, lamina cribrosa displacement, and scleral canal expansion. In addition, we examined the radial (maximum tension) and through-thickness (maximum compression) strains within the ONH tissues. Our models predicted that: 1) radial fibers reduced the posterior displacement of the lamina, especially at elevated IOP; 2) radial fibers reduced IOP-induced radial strain within the peripapillary sclera and retinal tissue; and 3) a combination of radial and circumferential fibers maintained strains within the ONH at a level similar to those conferred by circumferential fibers alone. In conclusion, radial fibers provide support for the posterior globe, additional to that provided by circumferential fibers. Most importantly, a combination of both fiber families can better protect ONH tissues from excessive IOP-induced deformation than either alone.

1. Introduction

The scleral canal in the posterior pole is often described as a “weak spot” in the globe (Fig. 1a). (Campbell et al., 2014; Sigal and Ethier, 2009) It is often further presumed that this weakness leads to concentrations of strain and stress that contribute to neural tissue damage and potentially to vision loss (Feola et al., 2016; Hua et al., 2018; Roberts et al., 2010b; Sigal and Ethier, 2009; Sigal et al., 2004, 2014b; Voorhees et al., 2017c). This could be the case if the posterior sclera was mechanically simple, such as constituted of linear, isotropic and

homogeneous materials. However, this is not the case. Studies have shown that the posterior sclera has complex architecture and mechanical properties (Boote et al., 2020; Coudrillier et al., 2012; Ethier et al., 2004; Jan et al., 2015, 2017). One of the most prominent features of posterior sclera architecture is a circumferential ring of collagen fibers surrounding the scleral canal. This ring has been reported in eyes of human (Brown et al., 2012; Coudrillier et al., 2012, 2013, 2015; Gogola et al., 2018; Markov et al., 2018; Pijanka et al., 2012, 2013; Zhang et al., 2015; Zhou et al., 2019b), monkey (Girard et al., 2009a, 2009c; Gogola et al., 2018), pig (Gogola et al., 2018), cow (Gogola et al., 2018), goat

* Corresponding author. Laboratory of Ocular Biomechanics, Department of Ophthalmology, University of Pittsburgh School of Medicine, 203 Lothrop Street, Eye and Ear Institute, Room 930, Pittsburgh, PA 15213, USA.

E-mail address: ian@ocularbiomechanics.com (I.A. Sigal).

<https://doi.org/10.1016/j.exer.2020.108188>

Received 24 June 2020; Received in revised form 22 July 2020; Accepted 6 August 2020

(Gogola et al., 2018), sheep (Gogola et al., 2018; Jan et al., 2017), and rat (Baumann et al., 2014; Girard et al., 2011). Computational models suggest that a posterior sclera with circumferential fibers is much more effective than one with randomly oriented fibers in providing mechanical support to the scleral canal. Specifically, the ring of fibers is thought to reduce the scleral canal expansion induced by elevated intraocular pressure (IOP), and with this the mechanical insult to the neural tissues within the canal (Campbell et al., 2015; Coudrillier et al., 2013; Girard et al., 2009b; Voorhees et al., 2018; Zhang et al., 2015).

We recently used polarized light microscopy to map the architecture of the peripapillary sclera at micron-scale resolution (Gogola et al., 2018; Jan et al., 2017). We found three distinct collagen organizations: the expected circumferential fibers proximal to the canal, unaligned “random” fibers, also previous described (Yang et al., 2018), and in the innermost peripapillary sclera (closest to the choroid) a family of collagen fibers aligned radially from the scleral canal (Fig. 1b). These radial fibers form a layer spanning 10–20% of the thickness of the peripapillary sclera, overlap with circumferential fibers in the region immediately adjacent to the canal, and extend at least 3 mm from the canal. We have observed these radial fibers in every eye we have studied, from sheep, monkey, pig, cow, goat, and human (Gogola et al., 2018; Jan et al., 2017). Others have also observed radial fibers in human eyes, both normal and with glaucoma, using wide-angle x-ray scattering (Pijanka et al., 2015). The prevalence of radial fibers and their proximity and organization tied to the scleral canal suggest that they may play a role in scleral canal and overall optic nerve head (ONH) biomechanics.

While a great deal of attention has been devoted to understanding the role of circumferential fibers on scleral canal biomechanics (Campbell et al., 2015; Coudrillier et al., 2013; Girard et al., 2009b; Voorhees et al., 2018; Zhang et al., 2015), the role of radial fibers has not been studied in nearly as much detail (Girard et al., 2009b; Grytz et al., 2020; Voorhees et al., 2018). Our goal was to determine the role of these radial fibers in the sensitivity of scleral canal biomechanics to acute increases in IOP. We hypothesized that radial fibers provide support for the posterior pole, additional to that provided by circumferential fibers, dampening the IOP-related biomechanical insult to the tissues of the

ONH and reducing the risk of damage.

2. Methods

We followed the same general approach as other studies of the role of sclera properties on the ONH (Feola et al., 2016; Girard et al., 2009b; Hua et al., 2018; Sigal et al., 2004, 2005a; Voorhees et al., 2016). Briefly, we created seven finite element models of the posterior pole of the eye with various combinations of radial and circumferential fibers. For each model, we simulated the biomechanical effects of normal (15 mmHg) or elevated (30 mmHg) IOP. Analyzing the set of models, we determined the role that each family of fibers – circumferential, radial, and combinations of them, have on IOP-induced deformation of the posterior sclera and ONH. The rationale for these key assumptions and implications are addressed later in the Discussion.

2.1. Model geometry

Based on the anatomy of the monkey eye (Roberts et al., 2010a), the posterior pole of the eye was modeled as a hemisphere with an inner radius of 10 mm and a constant thickness of 0.5 mm (Fig. 2a). The model was partitioned to represent various tissues (Fig. 2b). The region closest to the axis of symmetry with a radius of 0.8 mm represented the scleral canal, containing the lamina cribrosa (LC, 0.2 mm thick) and the pre- and post-laminar neural tissues (0.1 mm and 0.2 mm thick, respectively). The region adjacent to the canal had five layers, each 0.1 mm thick. The four outer layers were modeled as sclera and the innermost one as tissue that in this work we refer to as “retina”. Although we use the term “retina” for simplicity, similar to other studies (Hua et al., 2018; Sigal et al., 2004), it is important to consider that it represents both the retina and other neural tissues, as well as the choroid. The ring surrounding the canal with a width of 0.8 mm was defined as the peripapillary region, including the peripapillary sclera and retinal tissue.

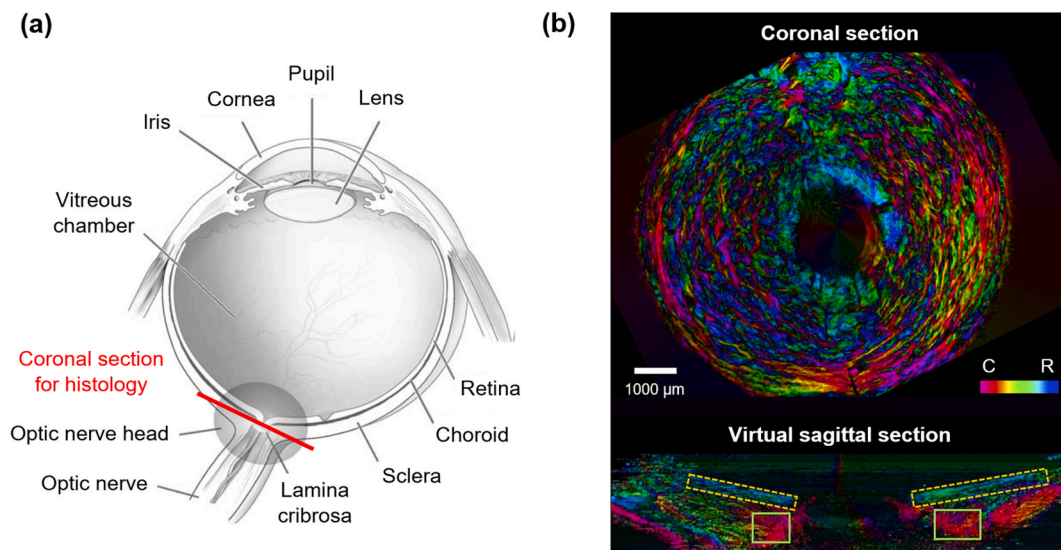


Fig. 1. (a) Anatomy of the eye in sagittal cross-section. Adapted from a diagram by the National Eye Institute. (b) Coronal (top) and sagittal (bottom) views of a human peripapillary sclera visualized on the submicrometer scale using polarized light microscopy (Jan et al., 2015). Following a process previously described (Gogola et al., 2018), a posterior pole was serially sectioned coronally. All the sections through the ONH were imaged, and a representative one selected to show. The sections were assembled into a stack and a virtual sagittal section created. In each image, colors indicate local fiber orientation in polar coordinates (C – Circumferential, R – Radial) in the section plane, whereas pixel intensity is proportional to collagen fiber density. Circumferential fibers can be identified by their red colors (green solid rectangles) and are adjacent to the scleral canal, in the more exterior sclera. Radial fibers can be identified by the blue and cyan colors (yellow dashed rectangles). Radial fibers form a layer spanning 10–20% of the thickness of the peripapillary sclera, overhang the circumferential fibers in the most anterior region immediately adjacent to the canal, and extend from the canal to the edge of the section. (For interpretation of the references to color in this figure legend, the reader is referred to the Web version of this article.)

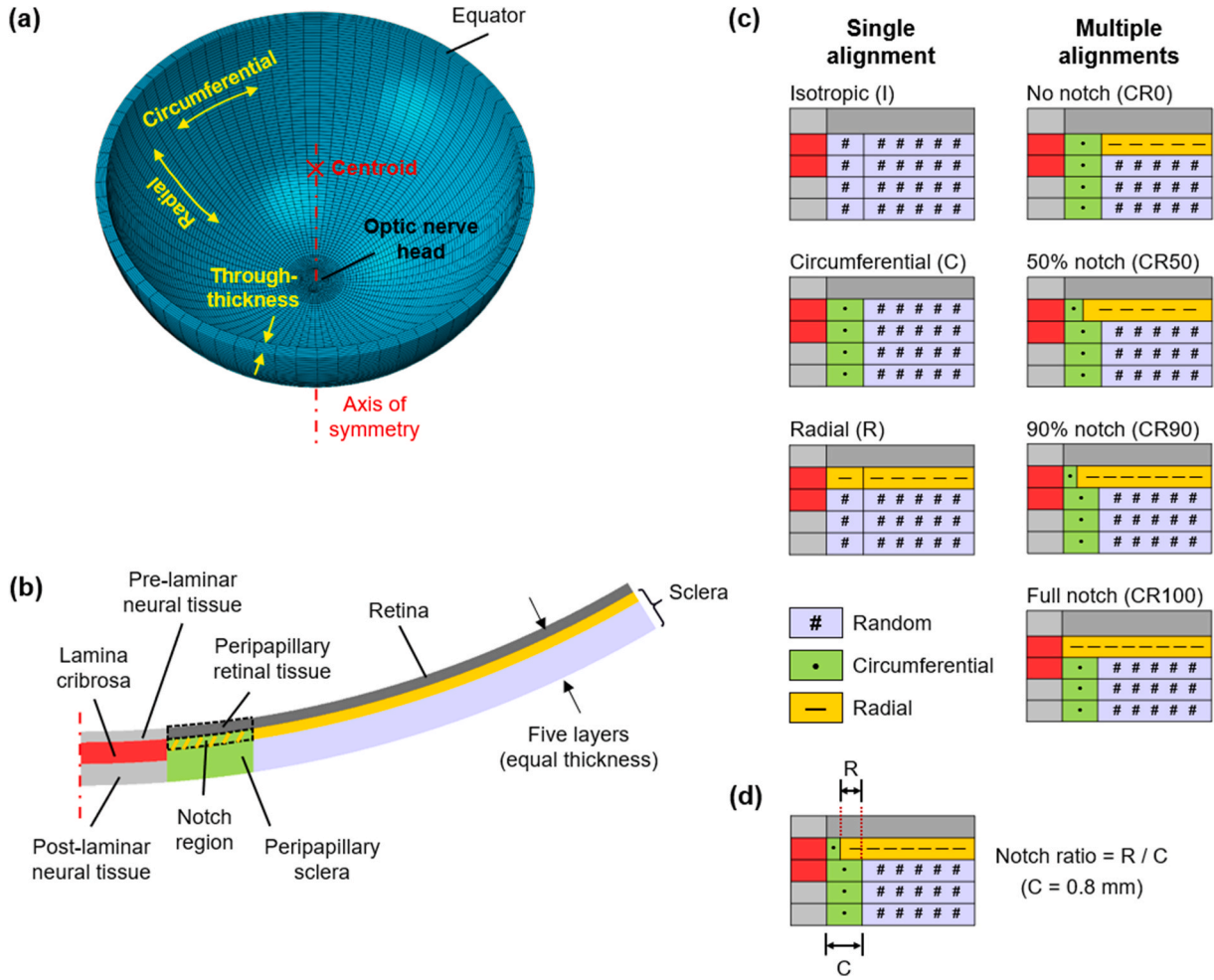


Fig. 2. (a) Generic model geometry of the posterior pole. Arrows indicate the circumferential, radial, and through-thickness directions, respectively. (b) Close-up of the optic nerve head region illustrating the tissues modeled. Shown is a cross section of an axially symmetric model. (c) Schematic illustration of the seven models with various scleral collagen fiber orientations. Regions of radial fibers are shaded in yellow with a “-” symbol, circumferential fibers in green with a “•” symbol, and randomly oriented fibers in light blue with a “#” symbol. Models CR0, CR50, CR90 and CR100 vary in the notch or the overlap between radial and circumferential fibers. (d) The notch ratio (range 0–100%) was calculated as the ratio of the overlap length of radial fibers in the peripapillary sclera region to the width of the circumferential ring. (For interpretation of the references to color in this figure legend, the reader is referred to the Web version of this article.)

2.2. Tissue mechanical properties

Tissues were modeled as hyperelastic, fiber-reinforced composites of the form utilized previously (Voorhees et al., 2017c). Briefly,

$$W = W_{Fiber} + W_{Ground} \quad (1)$$

where W was the total strain energy density, W_{Fiber} was the strain energy density of the anisotropic components such as fibers (collagen fibers for the sclera and LC beams or cytoskeletal filaments for the neural tissues), and W_{Ground} was the isotropic strain energy density of the ground substance. The strain energy density of a fiber was modeled using an exponential power law with the form

$$W_{Fiber} = \frac{\xi}{2\alpha} \left(\exp \left[\alpha (\lambda_n^2 - 1)^2 \right] - 1 \right) \quad (2)$$

where ξ was a linear material constant defining the linear stiffness of fibers, α was a non-linear material constant that governed how the stiffness of the fibers changed with the stretch of the fiber, and λ_n was the fiber stretch. The strain energy density for all fibers was then calculated as the sum of the strain energy density for individual fibers using the equation

$$W_{Fiber} = \int_{-\pi}^{\pi} H(\lambda_n - 1) \cdot p(\theta_n) \cdot W_{Fiber} \cdot d\theta_n \quad (3)$$

where H was a Heaviside function used to ensure that fibers were unstressed in compression, p was the probability density function used to describe the relative number of fibers with a given orientation, and θ_n was the orientation of an individual fiber. The strain energy density equation for the ground material was modeled as a Mooney-Rivlin solid which has the form

$$W_{Ground} = C_1(I_1 - 3) + C_2(I_2 - 3) + \frac{1}{2}K(\ln J)^2 \quad (4)$$

where C_1 and C_2 were material constants defining the stiffness of the material, I_1 and I_2 were the first and second invariants of the right Cauchy-Green deformation tensor (non-directional measures of material deformation), K was the bulk modulus which defined the compressibility of the material, and J was the Jacobian of the deformation gradient, which was a measure of the volume change of the material. For the collagenous tissues (sclera and LC), the parameter C_2 was set to zero, which is analogous to a neo-Hookean formulation.

Similar to previous finite element models (Feola et al., 2016; Girard et al., 2009b; Hua et al., 2017; Sigal et al., 2004, 2005a; Voorhees et al.,

Table 1

Mechanical properties specified for the sclera, lamina cribrosa and neural tissues (including the retina, and pre- and post-laminar neural tissues).

Parameters	Sclera	Lamina cribrosa	Neural tissues
ξ – Fiber stiffness (kPa)	1600	400	69.4
α – Fiber non-linearity	120	120	1
C_1 – 1st Mooney-Rivlin constant (kPa)	150	37.5	0.876
C_2 – 2nd Mooney-Rivlin constant (kPa)	0	0	0.614
K – Bulk modulus (kPa)	5000	1250	41.2

2017b, 2017c), the collagenous tissues (sclera and LC) were modeled using a nearly incompressible constitutive formulation, and therefore the bulk modulus does not directly correspond to the compressibility of the tissue. Instead, it acts as a penalty factor that helps define how strict the incompressibility constraint is enforced. The values selected provided reliable model convergence while keeping volume changes low. The neural tissues (retina, pre- and post-laminar neural tissues) were modeled as compressible, which allowed for changes in axoplasmic and blood volumes. The bulk modulus for the neural tissues was the one that Galle and colleagues obtained by fitting experimental data (Galle et al., 2010).

The hyperelastic parameters for the sclera were determined by fitting experimental data obtained from human sclera via inflation testing (Coudrillier et al., 2013), and those for the neural tissues were based on guinea pig white matter (Galle et al., 2010). Equivalent experimentally-measured LC properties are not available. Thus, we assigned the LC properties based on the reported average laminar connective tissue volume fraction (Roberts et al., 2010a). Specifically, this meant that the LC hyperelastic parameters were such that the LC strain energy density was one-fourth that of the sclera. For simplicity, we used a single set of parameters for the whole LC. A summary of tissue mechanical properties is listed in Table 1.

The collagen fibers were modeled using a 3D π -periodic von Mises distribution with a concentration parameter k . High values of k represented highly aligned fibers, whereas $k = 0$ represented a perfectly uniform distribution of fibers, i.e., unaligned “random” fibers. For the neural tissues in the retina, we assumed that the axons are well aligned, and therefore assigned the same degree of alignment parameter as the radial fibers in the sclera ($k = 2$). For the pre- and post-laminar neural tissues, we assumed that fibers were aligned anteriorly-posteriorly. The collagenous tissues, sclera and LC, were initially assigned random fibers

($k = 0$). For the parametric analysis the orientation and degree of alignment of various regions of the sclera were varied as detailed below.

2.3. Parametric studies

We created seven models with scleral collagen fibers organized in the following ways (Fig. 2c):

- Model I (from Isotropic): the simplest case, with the sclera assumed to be isotropic with no preferential orientation ($k = 0$). This is closest to the isotropic sclera in several previous studies (Bellezza et al., 2000; Hua et al., 2017, 2018; Norman et al., 2011; Sigal et al., 2004; Voorhees et al., 2016).
- Model C (from Circumferential): a model with a ring of fibers around the canal, with the peripapillary sclera assumed to be anisotropic in the circumferential direction ($k = 2$) (Coudrillier et al., 2013; Feola et al., 2016; Grytz et al., 2014, 2020; Voorhees et al., 2018; Zhang et al., 2015; Zhou et al., 2019a).
- Model R (from Radial): a model incorporating only radial fibers in the innermost sclera. Specifically, we assumed the innermost layer of the sclera to be anisotropic in the radial direction ($k = 2$) (Girard et al., 2009b; Grytz et al., 2020; Voorhees et al., 2018).
- Models CR0, CR50, CR90 and CR100 (from Circumferential and Radial): To account for all three tissue regions observed experimentally (Gogola et al., 2018). Models vary in the details of the “notch” region of overlap between radial and circumferential fibers. Specifically, the number refers to the percent of overlap length of radial fibers in the peripapillary sclera region to the width of the circumferential ring (Fig. 2d). In the extreme cases the radial fibers insert directly into the LC (CR100) or there is a full-width ring between radial fibers and canal (CR0). CR90 is likely the closest to our observations from histology (Gogola et al., 2018), although the anatomy varies substantially between eyes and species.

2.4. Boundary conditions

The models, as constructed, represented the posterior pole without IOP. Our goal was to understand the impact of radial fibers on the ONH biomechanical environment. It seems plausible that these fibers could play a role at all levels of IOP, or, alternatively, only at normal or only at elevated IOPs. Thus, we simulated the effects of increasing IOP from 0 to a normal 15 mmHg, and from 15 mmHg to an elevated 30 mmHg. The

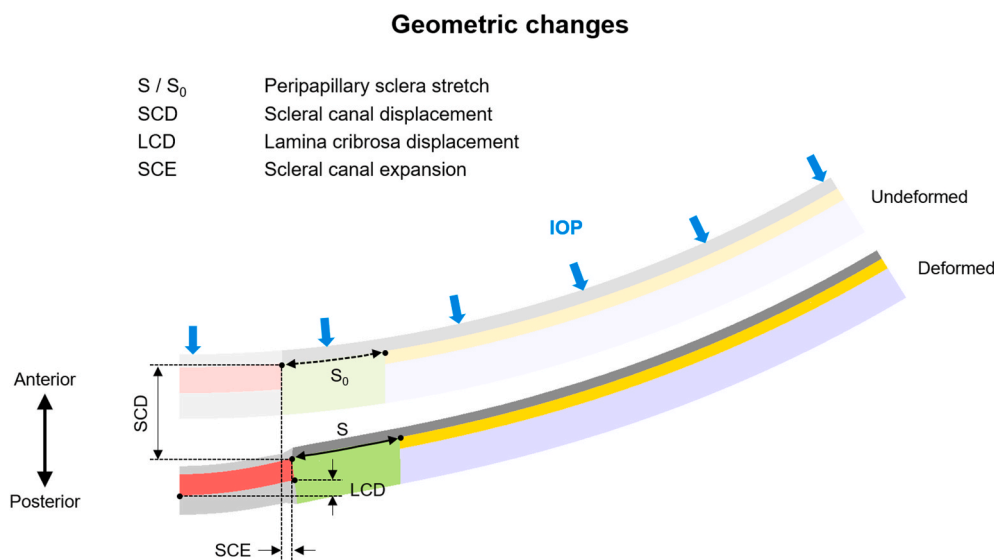


Fig. 3. Schematics of the optic nerve head region in the undeformed and deformed configurations to explain how the four geometric changes were calculated. The four geometric changes considered were the peripapillary sclera stretch, scleral canal displacement, lamina cribrosa displacement, and scleral canal expansion. We also quantified IOP-induced radial (maximum tension) and through-thickness (maximum compression) strains within the optic nerve head tissues. We refer readers to Fig. 2a for the direction conventions.

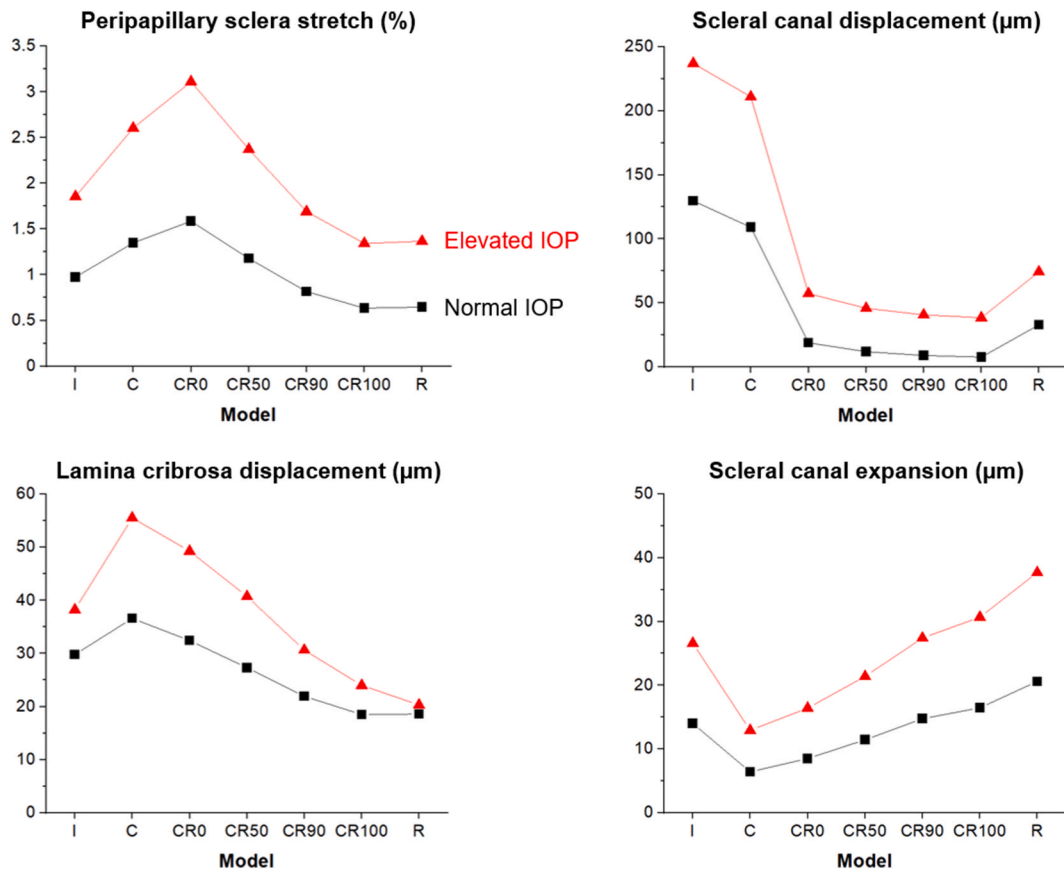


Fig. 4. Effects of collagen fiber orientations on the four geometric measures at normal (15 mmHg) and elevated (30 mmHg) IOPs. Note that there are no intermediate values between models and lines are added for visualization purposes only to help discern trends. Among all the models considered, Model C had the smallest scleral canal expansion and the largest lamina cribrosa displacement at both IOPs, whereas the opposite was observed with Model R. A good balance of IOP-induced geometric changes was reached by the models with a combination of both fiber families (Models CR0, CR50, CR90 and CR100). The notch ratio of radial fibers determined the combined effects of radial and circumferential fibers. A larger ratio made the combined effects closer to those of radial fibers (Model R), whereas a smaller one closer to those of circumferential fibers (Model C). For Model R, the lamina cribrosa displacement increased only by 9% as IOP doubled. This suggests that radial fibers are more efficient in reducing the lamina cribrosa displacement at elevated IOP.

nodes on the equator were constrained to deform so that they remained on the equatorial plane, as done previously (Hua et al., 2018; Sigal et al., 2004).

2.5. Solutions

All models were solved using FEBio v2.9.1 with eight-node hexahedral elements (Maas et al., 2012). Convergence tests were performed and adequate accuracy (relative strain differences under 1%) was

achieved with an averaged element length in the ONH and peripapillary sclera of 0.1 mm.

2.6. Outcome measures

We selected a set of outcome measures based on those that we (Hua et al., 2018; Sigal et al., 2004, 2011a, 2011b, 2007), and others (Coudrillier et al., 2012, 2013; Girard et al., 2009b; Ling et al., 2019; Ma et al., 2019, 2020; Midgett et al., 2020; Murienne et al., 2015; Pavlatos

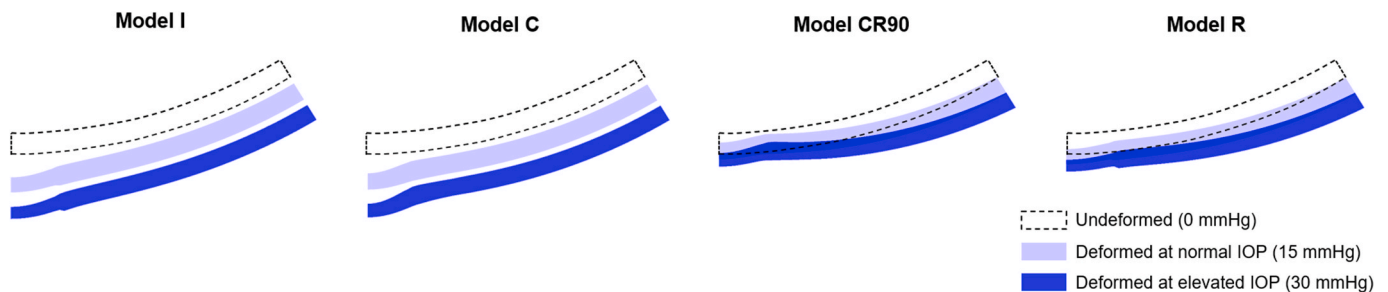


Fig. 5. An illustration of how the models displaced and deformed with the increases in IOP. Shown are computed deformations (exaggerated five times) for Models I, C, CR90 and R as IOP increased from 0 mmHg (dashed black lines show the model outline) to 15 mmHg (normal, light blue) and 30 mmHg (elevated, dark blue), respectively. Radial fibers (Models CR90 and R) are efficient in reducing IOP-induced posterior displacement of the scleral canal and lamina cribrosa. (For interpretation of the references to color in this figure legend, the reader is referred to the Web version of this article.)

At normal IOP (15 mmHg)

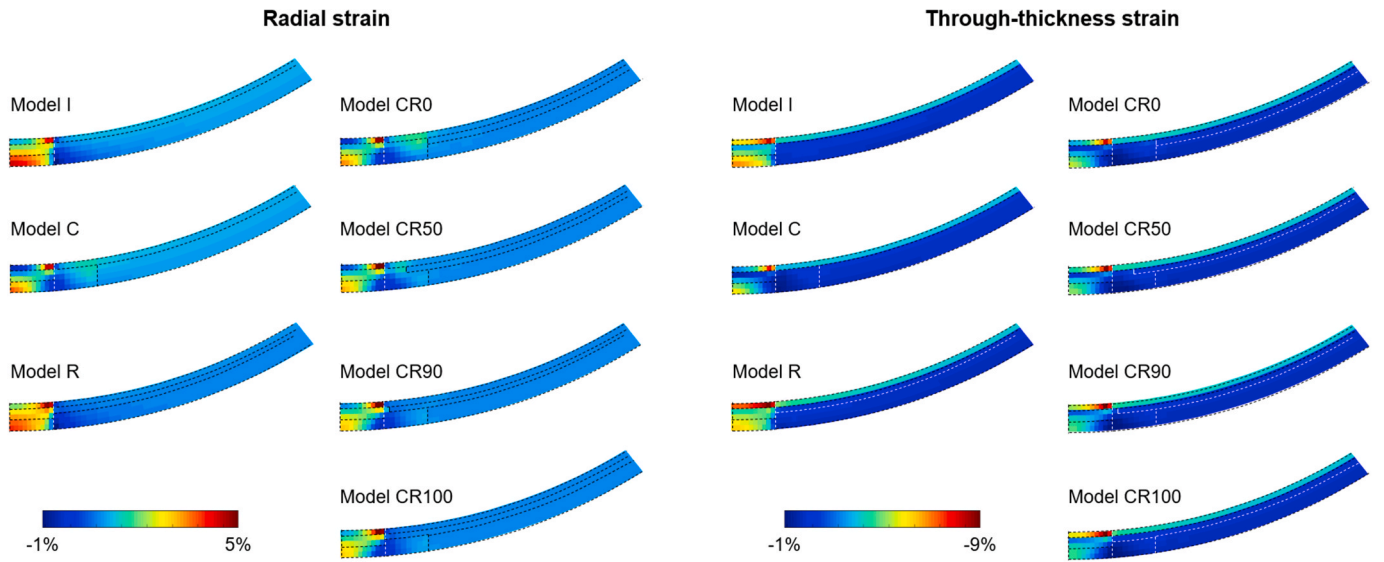


Fig. 6. Contour plots of radial and through-thickness strains at normal IOP (15 mmHg). To simplify comparisons, the strains are shown in the undeformed geometry. Dashed lines were added to help discern tissue boundaries, in black or white depending on the contour levels. There were three “hot spots” of strain: in the scleral canal at the LC and post-laminar tissues, in the peripheral pre-laminar tissues, and in the most anterior peripapillary region. In general, the strains in Model C were smaller than those in Model I. Models CR0, CR50, CR90 and CR100 maintained strains within the ONH at a level similar to those in Model C in the canal and slightly lower in the sclera. Overall, the through-thickness strain showed similar dependence on fiber orientations to radial strain.

et al., 2016, 2018), have postulated are biologically important or because they are clinically observable. We divided the outcome measures into the following categories.

Geometric changes

- Peripapillary sclera stretch: measured as the extension of the curve length of the anterior surface of the peripapillary sclera (Fig. 3). Note the peripapillary sclera stretch is similar to strain measures in that it represents a change in length. However, instead of being a measure

at a point, like strain is, the peripapillary sclera stretch represents the average stretch in the anterior surface of the peripapillary sclera.

- Scleral canal displacement: measured as changes in the anterior-posterior position of the anterior scleral canal opening with respect to the centroid of the globe (Girard et al., 2009b; Hua et al., 2018; Sigal et al., 2004).
- Lamina cribrosa displacement: measured as changes in the anterior-posterior position of the center of the posterior LC surface with

At normal IOP (15 mmHg)

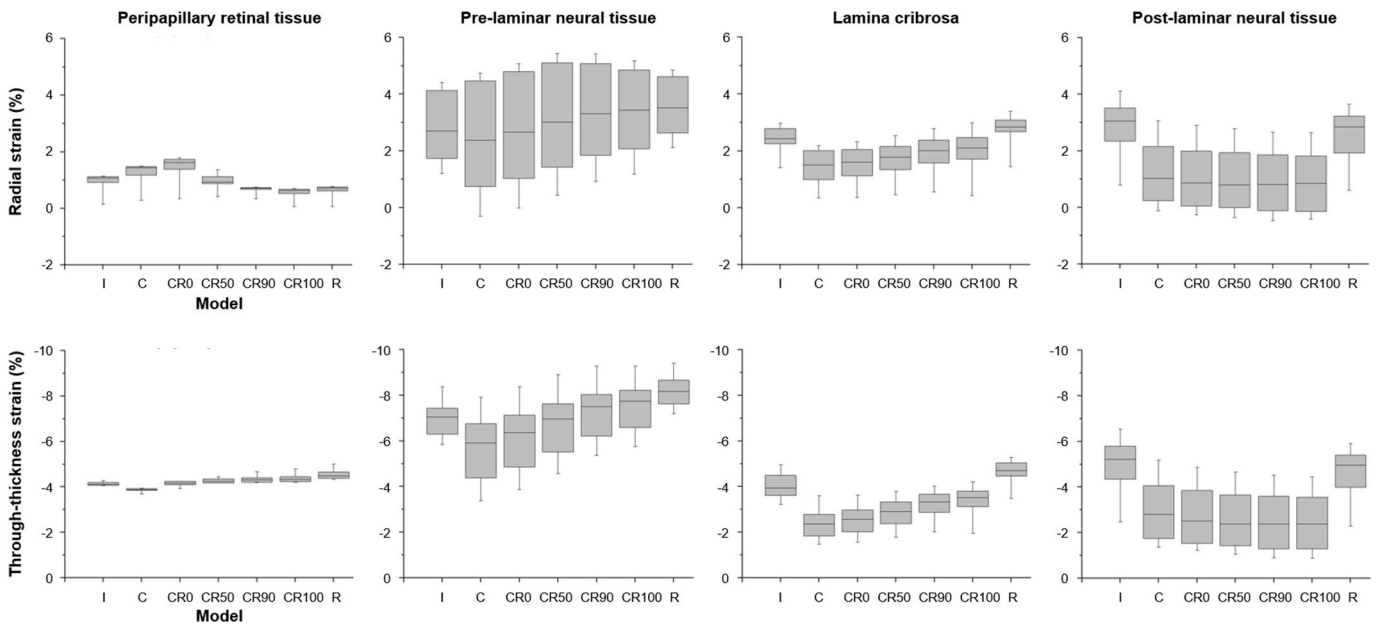


Fig. 7. Box plots of radial and through-thickness strains within four regions of the ONH at normal IOP (15 mmHg). The four regions were the peripapillary retinal tissue, pre-laminar neural tissue, lamina cribrosa, and post-laminar neural tissue. Consistent with the observations in Fig. 6, Models CR0, CR50, CR90 and CR100 maintained strains within the four regions of the ONH at a level similar to those in Model C.

respect to the posterior lamina insertion into the sclera (Girard et al., 2009b; Hua et al., 2018; Sigal et al., 2004, 2011a, 2011b).

- Scleral canal expansion: measured as changes in the canal diameter at the anterior scleral canal opening (Coudrillier et al., 2013; Girard et al., 2009b; Hua et al., 2018; Sigal et al., 2004, 2011a, 2011b).

Strains

- Radial strain: a measure of IOP-induced maximum tension of ONH tissues. See Fig. 2a for the direction conventions (Coudrillier et al., 2012; Girard et al., 2009b; Ling et al., 2019; Ma et al., 2019, 2020; Midgett et al., 2020; Murienne et al., 2015; Pavlatos et al., 2016, 2018; Sigal et al., 2007).
- Through-thickness strain: a measure of IOP-induced maximum compression of ONH tissues (Ma et al., 2019, 2020; Pavlatos et al., 2016, 2018; Sigal et al., 2007).

We computed the distributions of each of the strains within four regions of the ONH, *i.e.*, the peripapillary retinal tissue, pre-laminar neural tissue, lamina cribrosa, and post-laminar neural tissue. These distributions were characterized by the median and peak. The volume-weighted 95th and 5th percentiles were used as the definition of the peak value of radial and through-thickness strains, respectively, to reduce the influence of possible numerical artifacts (for example, from artificially sharp geometries or transitions in tissue mechanical properties) or of regions too small to have a physiologic significance. Note also that terminology sometimes varies between studies. For example, the term “radial” is sometimes used to refer to the direction from the center of the globe, akin to what we call “through-thickness”. Herein we followed the terminology in our studies of ONH and sclera microstructure (Gogola et al., 2018; Jan et al., 2017).

3. Results

The effects of collagen fiber orientations on the four geometric measures are shown in Fig. 4. Overall, there were substantial effects of the fiber orientations on stretch, displacement, and expansion of tissues. An illustration of how the models displaced and deformed with increases

in IOP is shown in Fig. 5. The images show that circumferential and radial fibers have distinct effects on the posterior pole and ONH response to IOP, and are neither independent nor opposite.

The distributions of radial and through-thickness strains predicted at normal IOP are shown as contour plots in Fig. 6. Corresponding box plots are shown in Fig. 7. There were three “hot spots” of strain: in the scleral canal at the LC and post-laminar tissues, in the peripheral pre-laminar tissues, and in the most anterior peripapillary region. Models CR0, CR50, CR90 and CR100 maintained strains within the four regions of the ONH at a level similar to those in Model C in the canal and slightly lower in the sclera. Overall, the through-thickness strain showed similar dependence on fiber orientations to radial strain.

Contour and box plots at elevated IOP are shown in Figs. 8 and 9, respectively. Distribution patterns of the strains were similar between normal and elevated IOPs. At elevated IOP, Model R had a lower peak radial strain within the pre-laminar neural tissue than Model C, whereas the opposite was observed at normal IOP. Not surprisingly, the magnitudes of the strains at elevated IOP were higher than at normal IOP. Due to the nonlinear mechanical properties, IOP doubling produced less than double deformations.

4. Discussion

Recent studies have demonstrated the existence of a family of fibers in the innermost sclera organized radially from the scleral canal (Boote et al., 2020; Gogola et al., 2018; Jan et al., 2017; Pijanka et al., 2015). Our goal was to determine the role of these radial fibers in the sensitivity of scleral canal biomechanics to acute increases in IOP. We have shown that, despite being less than 20% of the thickness of the peripapillary sclera, this layer of radial fibers has substantial effects on scleral canal biomechanics. Specifically, our models predicted that: 1) radial fibers reduced the posterior displacement of the lamina, especially at elevated IOP; 2) radial fibers reduced IOP-induced radial strain within the peripapillary sclera and retinal tissue; and 3) a combination of radial and circumferential fibers maintained strains within the ONH at a level similar to those conferred by circumferential fibers alone. Below we discuss each of these findings in detail.

Our models predicted that radial fibers reduced the posterior

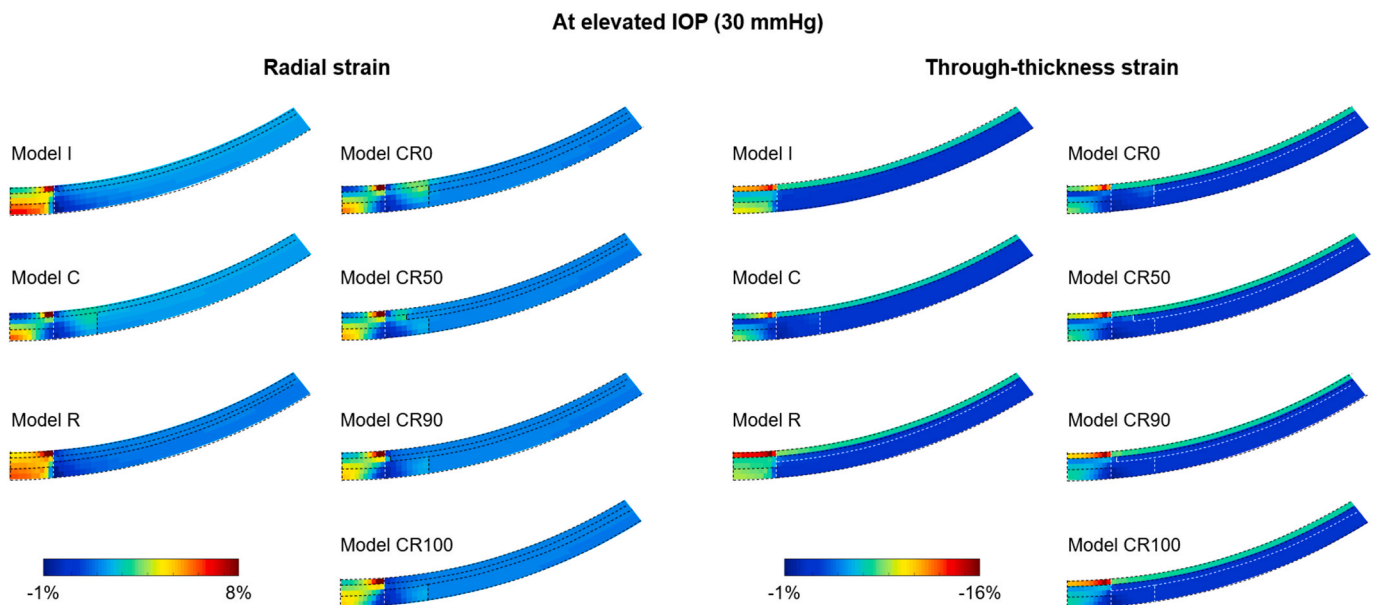


Fig. 8. Contour plots of radial and through-thickness strains at elevated IOP (30 mmHg). To simplify comparisons, strains are shown in the undeformed geometry. Dashed lines were added to help discern tissue boundaries, in black or white depending on the contour levels. Distribution patterns of the strains were similar between normal and elevated IOPs, although the strain magnitudes at elevated IOP were higher. Due to the nonlinear mechanical properties, IOP doubling produced less than double deformations.

At elevated IOP (30 mmHg)

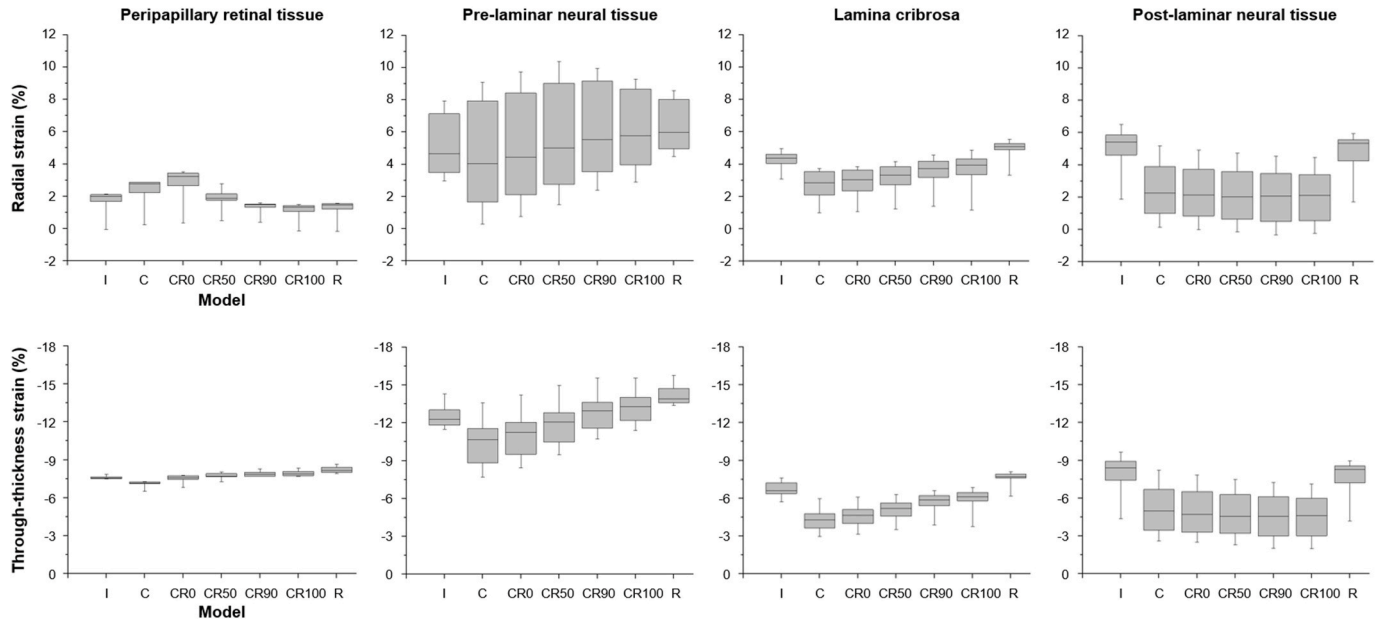


Fig. 9. Box plots of radial and through-thickness strains within four regions of the ONH at elevated IOP (30 mmHg). The formatting is the same as in Fig. 7. Again, distribution patterns of the strains were similar between normal and elevated IOPs. At elevated IOP, Model R had a lower peak radial strain within the pre-laminar neural tissue than Model C, whereas the opposite was observed at normal IOP.

displacement of the lamina, especially at elevated IOP. The implications of this can be better understood when considering a useful framework that has emerged in the past few years to describe lamina displacements resulting from increases in IOP. In this framework, overall lamina displacements are the result of the direct effects of IOP pushing the lamina posteriorly, and the indirect effects of IOP deforming the sclera, expanding the canal, which in turn pulls the lamina taut from the sides (Burgoyne and Downs, 2008; Girard et al., 2009b; Roberts et al., 2010a; Sigal and Ethier, 2009; Sigal et al., 2010b, 2011b; Yang et al., 2009). Within this framework, a simple reinforcement of the canal with circumferential fibers is efficient in reducing IOP-induced canal expansion (indirect effects of IOP). However, this is at the expense of inducing a large posterior displacement of the lamina (direct effects of IOP). This “disadvantage” of circumferential fibers can be counteracted by radial fibers, which allow the canal to expand substantially and pull the lamina taut from the sides, reducing its posterior displacement. Our results further suggest that a combination of both families of radial and circumferential fibers supports the posterior globe better than either alone. The notch ratio of radial fibers determined the combined effects of radial and circumferential fibers. A larger ratio made the combined effects closer to those of radial fibers, whereas a smaller one was closer to those of circumferential fibers. We analyzed histological sections of sheep posterior sclera and found that the physiological notch ratio of radial fibers was close to 90% (Model CR90) (Jan et al., 2017), indicating the combined effects were dominated by those of radial fibers.

Radial fibers reduced IOP-induced radial strain within the peripapillary sclera and retinal tissue. This strain is longitudinal to the axons, and potentially harmful. Our results demonstrate that radial fibers can protect the neural tissues of the retina surrounding the canal, complementing circumferential fibers that protect the neural tissues within the canal. Our results also show that, compared to a sclera with circumferential fibers alone, a sclera with radial fibers alone had a lower peak radial strain within the pre-laminar neural tissue at elevated IOP. This peak strain was located at the rim area of the pre-laminar neural tissue, adjacent to the peripapillary retinal tissue. Several studies have suggested that, in addition to the LC, the pre-laminar neural tissue rim may be another site of injury to the retinal ganglion cell axons in

glaucoma (Chauhan et al., 2013; Chen, 2009; Danthurebandara et al., 2015; Fortune et al., 2016; Gardiner et al., 2014; Lee et al., 2020). The level of strain likely increases the risk of axonal injury (Gennarelli et al., 1989; Kurtoglu et al., 2017; Lee et al., 2017; Margulies and Thibault, 1992). Hence, the advantage of radial fibers to reduce peak radial strain within the pre-laminar neural tissue rim at elevated IOP may play an important role in axonal protection.

A combination of radial and circumferential fibers maintained strains within the ONH at a level similar to those conferred by circumferential fibers alone. This suggests that the existence of radial fibers does not weaken the biomechanical support to the ONH provided by circumferential fibers. Strains within the LC increased with the notch ratio of radial fibers. Since the LC is the primary site of axonal injury to retinal ganglion cells in glaucoma (Minckler et al., 1977; Quigley, 1999, 2005), we hypothesize that this ratio may contribute to the predisposition of glaucoma. However, additional studies, *i.e.*, accurate measurements and comparison of the notch ratio of radial fibers between normal and glaucoma human eyes, are needed to test our hypothesis.

Although several studies have identified radially aligned collagen fibers in the innermost layer of the sclera (Boote et al., 2020; Gogola et al., 2018; Jan et al., 2017; Pijanka et al., 2015), to the best of our knowledge, there have been no systematic analysis of how these fibers affect the biomechanical environment within the scleral canal. We have demonstrated that radial fibers provide support for the posterior globe additional to that provided by circumferential fibers, and most importantly, that a combination of both fiber families can better protect ONH tissues from IOP-induced excessive deformation than either alone. Most numerical models of the posterior pole that consider scleral anisotropy, only incorporated circumferential fibers surrounding the canal (Campbell et al., 2015; Feola et al., 2016; Voorhees et al., 2017c, 2018; Wang et al., 2016; Zhang et al., 2015). To the best of our knowledge, the only numerical study incorporating both circumferential and radial fibers is that of Grytz and colleagues (Grytz et al., 2020). This study suggests that missing radial fibers could reduce the fidelity of the models for representing posterior pole response to IOP.

The numerical models presented in this work are a simplification of the ONH and posterior pole of the eye, in both anatomy and mechanical

properties. It follows the general idea of generic parametric models we have published previously (Sigal, 2009, 2011; Sigal et al., 2004, 2005a; Voorhees et al., 2016). Although the simplifications may not capture every aspect of the complex behavior of the ONH, they are well-suited to test the fundamental behavior of the parameters of interest, without the overlying complexity of inter-eye variability that the specimen-specific models imply (Sigal et al., 2005b, 2009a, b, 2010a; Sigal et al., 2010c). In addition, these simplifications help provide fundamental new insight into the mechanical behavior of the posterior pole of the eye that would be otherwise unobtainable through experiment. A thorough discussion of the limitations of this modeling approach can be found in our previous studies (Roberts et al., 2018; Sigal et al., 2004, 2005a, 2014a; Sigal and Ethier, 2009, 2007; Sigal and Grimm, 2012; Voorhees et al., 2016), and was recently discussed in detail (Roberts et al., 2018). Below, we summarize the limitations and considerations most relevant to this work.

First, our models only simulated the posterior pole of the eye, without including the anterior portion. It is possible that the deformation of the posterior pole is influenced by that of the anterior portion. We recently used high-field MRI to measure IOP-induced whole globe deformation (Voorhees et al., 2017a). Anterior bulging of the cornea and posterior bowing of the sclera were clearly observed, but changes in the equatorial diameter were minimal. This suggests that the deformation of the anterior pole diminishes towards the equator, and its influence on the deformation of the posterior pole should be negligible.

Second, although our models incorporated depth-dependent variations in collagen fiber orientations, the degree of fiber alignment was simply assumed the same ($k = 2$). In future models, a physiological-based degree of fiber alignment, a feature that may contribute to the development and progression of glaucoma, should be taken into consideration (Danford et al., 2013; Pijanka et al., 2015; Yan et al., 2011).

Third, we assumed that radial fibers extended all the way to the equator. This assumption is based on our previous studies, where we reported that radial fibers extended out from near the canal to the edge of trephine sections (diameter: 8–14 mm) (Gogola et al., 2018; Jan et al., 2017). It remains unknown if they extend to the equator.

Fourth, we treated random fibers as an isotropic mixture. Using polarized light microscopy, we found that these fibers were actually interwoven and formed a basket-weave pattern (Jan et al., 2017; Yang et al., 2018). More complex models will be required to understand the implications of this interwoven architecture on scleral canal biomechanics (Wang et al., 2020).

Fifth, we derived neural tissue properties from guinea pig white matter and thus they are not exact for human eyes (Galle et al., 2010). The rationale for our choice has been illustrated previously (Voorhees et al., 2017b, 2017c). Experimental determination of neural tissue mechanical properties would improve future models and provide valuable insight into the mechanics of the ONH.

Sixth, our models account only for acute effects of IOP, and do not incorporate chronic effects, which could include remodeling (Grytz et al., 2012; Yang et al., 2017), compromised perfusion (Chuangsuwanich et al., 2016; Paula et al., 2017) and/or axoplasmic flow (Boote et al., 2020; Yang et al., 2017), or neural tissue loss. In addition, our models do not incorporate intracranial pressure changes (Feola et al., 2016; Hua et al., 2017, 2018), eye movements (Wang et al., 2016), and choroidal swelling (Feola et al., 2018), in which radial fibers may play a distinct role in ONH biomechanics. The models also do not consider prestresses (Grytz and Downs, 2013) or residual stresses or strains (Wang et al., 2015).

In conclusion, we have demonstrated that radial fibers provide support for the posterior globe additional to that provided by circumferential fibers. Most importantly, we show that a combination of both fiber families can better protect ONH tissues from excessive IOP-induced deformation than either alone. Several techniques for neuroprotection via manipulation of scleral mechanical properties are in development

(Campbell et al., 2017; Quigley and Cone, 2013). An understanding of the complex characteristics of the sclera and their interactions on scleral canal biomechanics is essential to optimize these treatments.

Funding support

National Institutes of Health R01-EY023966, R01-EY028662, P30-EY008098 and T32-EY017271 (Bethesda, MD), the Eye and Ear Foundation (Pittsburgh, PA) and Research to Prevent Blindness (support to the Department of Ophthalmology, University of Pittsburgh and to the Department of Ophthalmology, NYU Langone Health, NYU Grossman School of Medicine).

Declaration of competing interest

Dr. Voorhees was at the University of Pittsburgh when he contributed to this work. He is now at Johnson & Johnson. Dr. Schuman received royalties for intellectual property licensed by the Massachusetts Institute of Technology and Massachusetts Eye and Ear Infirmary to Zeiss, Inc.

References

- Baumann, B., Rauscher, S., Glösmann, M., Götzing, E., Pircher, M., Fialová, S., Gröger, M., Hitzberger, C.K., 2014. Peripapillary rat sclera investigated in vivo with polarization-sensitive optical coherence tomography. *Investig. Ophthalmol. Vis. Sci.* 55, 7686–7696.
- Bellezza, A.J., Hart, R.T., Burgoyne, C.F., 2000. The optic nerve head as a biomechanical structure: initial finite element modeling. *Investig. Ophthalmol. Vis. Sci.* 41, 2991–3000.
- Boote, C., Sigal, I.A., Grytz, R., Hua, Y., Nguyen, T.D., Girard, M.J.A., 2020. Scleral structure and biomechanics. *Prog. Retin. Eye Res.* 74, 100773.
- Brown, D.J., Jester, J.V., Reid, K., Minckler, D.S., 2012. Nonlinear optical (NLO) assessment of the human optic nerve head (ONH). *Investig. Ophthalmol. Vis. Sci.* 53, 3934–3934.
- Burgoyne, C.F., Downs, J.C., 2008. Premise and prediction—how optic nerve head biomechanics underlies the susceptibility and clinical behavior of the aged optic nerve head. *J. Glaucoma* 17, 318–328.
- Campbell, I.C., Coudrillier, B., Ethier, C.R., 2014. Biomechanics of the posterior eye: a critical role in health and disease. *J. Biomech. Eng.* 136, 021005.
- Campbell, I.C., Coudrillier, B., Mensah, J., Abel, R.L., Ethier, C.R., 2015. Automated segmentation of the lamina cribrosa using Frangi's filter: a novel approach for rapid identification of tissue volume fraction and beam orientation in a trabeculated structure in the eye. *J. R. Soc. Interface* 12, 20141009.
- Campbell, I.C., Hannon, B.G., Read, A.T., Sherwood, J.M., Schwanner, S.A., Ethier, C.R., 2017. Quantification of the efficacy of collagen cross-linking agents to induce stiffening of rat sclera. *J. R. Soc. Interface* 14, 20170014.
- Chauhan, B.C., O'Leary, N., AlMobarak, F.A., Reis, A.S., Yang, H., Sharpe, G.P., Hutchison, D.M., Nicoleta, M.T., Burgoyne, C.F., 2013. Enhanced detection of open-angle glaucoma with an anatomically accurate optical coherence tomography-derived neuroretinal rim parameter. *Ophthalmology* 120, 535–543.
- Chen, T.C., 2009. Spectral domain optical coherence tomography in glaucoma: qualitative and quantitative analysis of the optic nerve head and retinal nerve fiber layer (an AOS thesis). *Trans. Am. Ophthalmol. Soc.* 107, 254–281.
- Chuangsuwanich, T., Birgersson, K.E., Thiery, A., Thakku, S.G., Leo, H.L., Girard, M.J., 2016. Factors influencing lamina cribrosa microcapillary hemodynamics and oxygen concentrations. *Investig. Ophthalmol. Vis. Sci.* 57, 6167–6179.
- Coudrillier, B., Boote, C., Quigley, H.A., Nguyen, T.D., 2013. Scleral anisotropy and its effects on the mechanical response of the optic nerve head. *Biomech. Model. Mechanobiol.* 12, 941–963.
- Coudrillier, B., Pijanka, J.K., Jefferys, J.L., Goel, A., Quigley, H.A., Boote, C., Nguyen, T. D., 2015. Glaucoma-related changes in the mechanical properties and collagen micro-architecture of the human sclera. *PLoS One* 10, e0131396.
- Coudrillier, B., Tian, J., Alexander, S., Myers, K.M., Quigley, H.A., Nguyen, T.D., 2012. Biomechanics of the human posterior sclera: age- and glaucoma-related changes measured using inflation testing. *Investig. Ophthalmol. Vis. Sci.* 53, 1714–1728.
- Danford, F.L., Yan, D., Dreier, R.A., Cahir, T.M., Girkin, C.A., Geest, J.P.V., 2013. Differences in the region- and depth-dependent microstructural organization in normal versus glaucomatous human posterior sclerae. *Investig. Ophthalmol. Vis. Sci.* 54, 7922–7932.
- Danthurebandara, V.M., Sharpe, G.P., Hutchison, D.M., Dennis, J., Nicoleta, M.T., McKendrick, A.M., Turpin, A., Chauhan, B.C., 2015. Enhanced structure–function relationship in glaucoma with an anatomically and geometrically accurate neuroretinal rim measurement. *Investig. Ophthalmol. Vis. Sci.* 56, 98–105.
- Ethier, C.R., Johnson, M., Ruberti, J., 2004. Ocular biomechanics and biotransport. *Annu. Rev. Biomed. Eng.* 6, 249–273.
- Feola, A.J., Myers, J.G., Raykin, J., Mulugeta, L., Nelson, E.S., Samuels, B.C., Ethier, C.R., 2016. Finite element modeling of factors influencing optic nerve head deformation due to intracranial pressure. *Investig. Ophthalmol. Vis. Sci.* 57, 1901–1911.

- Feola, A.J., Nelson, E.S., Myers, J., Ethier, C.R., Samuels, B.C., 2018. The impact of choroidal swelling on optic nerve head deformation. *Investig. Ophthalmol. Vis. Sci.* 59, 4172–4181.
- Fortune, B., Reynaud, J., Hardin, C., Wang, L., Sigal, I.A., Burgoyne, C.F., 2016. Experimental glaucoma causes optic nerve head neural rim tissue compression: a potentially important mechanism of axon injury. *Investig. Ophthalmol. Vis. Sci.* 57, 4403–4411.
- Galle, B., Ouyang, H., Shi, R., Nauman, E., 2010. A transversely isotropic constitutive model of excised Guinea pig spinal cord white matter. *J. Biomech.* 43, 2839–2843.
- Gardiner, S.K., Ren, R., Yang, H., Fortune, B., Burgoyne, C.F., Demirel, S., 2014. A method to estimate the amount of neuroretinal rim tissue in glaucoma: comparison with current methods for measuring rim area. *Am. J. Ophthalmol.* 157, 540–549.
- Gennarelli, T., Thibault, L., Tipperman, R., Tomei, G., Sergot, R., Brown, M., Maxwell, W., Graham, D., Adams, J., Irvine, A., 1989. Axonal injury in the optic nerve: a model simulating diffuse axonal injury in the brain. *J. Neurosurg.* 71, 244–253.
- Girard, M.J., Dahlmann-Noor, A., Rayapureddi, S., Bechara, J.A., Bertin, B.M., Jones, H., Albon, J., Khaw, P.T., Ethier, C.R., 2011. Quantitative mapping of scleral fiber orientation in normal rat eyes. *Investig. Ophthalmol. Vis. Sci.* 52, 9684–9693.
- Girard, M.J., Downs, J.C., Bottlang, M., Burgoyne, C.F., Suh, J.-K.F., 2009a. Peripapillary and posterior scleral mechanics—part II: experimental and inverse finite element characterization. *J. Biomech. Eng.* 131, 051012.
- Girard, M.J., Downs, J.C., Burgoyne, C.F., Suh, J.-K.F., 2009b. Peripapillary and posterior scleral mechanics—part I: development of an anisotropic hyperelastic constitutive model. *J. Biomech. Eng.* 131, 051011.
- Girard, M.J., Suh, J.-K.F., Bottlang, M., Burgoyne, C.F., Downs, J.C., 2009c. Scleral biomechanics in the aging monkey eye. *Investig. Ophthalmol. Vis. Sci.* 50, 5226–5237.
- Gogola, A., Jan, N.-J., Lathrop, K.L., Sigal, I.A., 2018. Radial and circumferential collagen fibers are a feature of the peripapillary sclera of human, monkey, pig, cow, goat, and sheep. *Investig. Ophthalmol. Vis. Sci.* 59, 4763–4774.
- Grytz, R., Downs, J.C., 2013. A forward incremental prestressing method with application to inverse parameter estimations and eye-specific simulations of posterior scleral shells. *Comput. Methods Biomech. Biomed. Eng.* 16, 768–780.
- Grytz, R., Fazio, M.A., Girard, M.J., Libertaux, V., Bruno, L., Gardiner, S., Girkin, C.A., Downs, J.C., 2014. Material properties of the posterior human sclera. *Journal of the mechanical behavior of biomedical materials* 29, 602–617.
- Grytz, R., Krishnan, K., Whitley, R., Libertaux, V., Sigal, I.A., Girkin, C.A., Downs, J.C., 2020. A mesh-free approach to incorporate complex anisotropic and heterogeneous material properties into eye-specific finite element models. *Comput. Methods Appl. Mech. Eng.* 358, 112654.
- Grytz, R., Sigal, I.A., Ruberti, J.W., Meschke, G., Downs, J.C., 2012. Lamina cribrosa thickening in early glaucoma predicted by a microstructure motivated growth and remodeling approach. *Mech. Mater.* 44, 99–109.
- Hua, Y., Tong, J., Ghate, D., Kedar, S., Gu, L., 2017. Intracranial pressure influences the behavior of the optic nerve head. *J. Biomech. Eng.* 139, 031003.
- Hua, Y., Voorhees, A.P., Sigal, I.A., 2018. Cerebrospinal fluid pressure: revisiting factors influencing optic nerve head biomechanics. *Investig. Ophthalmol. Vis. Sci.* 59, 154–165.
- Jan, N.J., Grimm, J.L., Tran, H., Lathrop, K.L., Wollstein, G., Bilonick, R.A., Ishikawa, H., Kagemann, L., Schuman, J.S., Sigal, I.A., 2015. Polarization microscopy for characterizing fiber orientation of ocular tissues. *Biomed. Optic Express* 6, 4705–4718.
- Jan, N.J., Lathrop, K., Sigal, I.A., 2017. Collagen architecture of the posterior Pole: high-resolution wide field of view visualization and analysis using polarized light microscopy. *Invest. Ophthalmol. Vis. Sci.* 58, 735–744.
- Kurtoglu, E., Nakadate, H., Kikuta, K., Aomura, S., Kakuta, A., 2017. Uniaxial stretch-induced axonal injury thresholds for axonal dysfunction and disruption and strain rate effects on thresholds for mouse neuronal stem cells. *J. Biomech. Sci. Eng.* 12, 16–598.
- Lee, E.J., Han, J.C., Kee, C., 2017. A novel hypothesis for the pathogenesis of glaucomatous disc hemorrhage. *Prog. Retin. Eye Res.* 60, 20–43.
- Lee, E.J., Han, J.C., Kee, C., 2020. A neuroglia-based interpretation of glaucomatous neuroretinal rim thinning in the optic nerve head. *Prog. Retin. Eye Res.* 100840.
- Ling, Y.T.T., Shi, R., Midgett, D.E., Jefferys, J.L., Quigley, H.A., Nguyen, T.D., 2019. Characterizing the collagen network structure and pressure-induced strains of the human lamina cribrosa. *Invest. Ophthalmol. Vis. Sci.* 60, 2406–2422.
- Ma, Y., Pavlatos, E., Clayson, K., Kwok, S., Pan, X., Liu, J., 2020. Three-dimensional inflation response of porcine optic nerve head using high-frequency ultrasound elastography. *J. Biomech. Eng.* 142, 051013.
- Ma, Y., Pavlatos, E., Clayson, K., Pan, X., Kwok, S., Sandwisch, T., Liu, J., 2019. Mechanical deformation of human optic nerve head and peripapillary tissue in response to acute IOP elevation. *Investig. Ophthalmol. Vis. Sci.* 60, 913–920.
- Maas, S.A., Ellis, B.J., Ateshian, G.A., Weiss, J.A., 2012. FEBio: finite elements for biomechanics. *J. Biomech. Eng.* 134, 011005.
- Margulies, S.S., Thibault, L.E., 1992. A proposed tolerance criterion for diffuse axonal injury in man. *J. Biomech.* 25, 917–923.
- Markov, P.P., Eliasy, A., Pijanka, J.K., Htoon, H.M., Paterson, N.G., Sorensen, T., Elsheikh, A., Girard, M.J., Boote, C., 2018. Bulk changes in posterior scleral collagen microstructure in human high myopia. *Mol. Vis.* 24, 818.
- Midgett, D.E., Jefferys, J.L., Quigley, H.A., Nguyen, T.D., 2020. The inflation response of the human lamina cribrosa and sclera: analysis of deformation and interaction. *Acta Biomater.* 106, 225–241.
- Minckler, D., Bunt, A., Johanson, G., 1977. Orthograde and retrograde axoplasmic transport during acute ocular hypertension in the monkey. *Investig. Ophthalmol. Vis. Sci.* 16, 426–441.
- Murienne, B.J., Jefferys, J.L., Quigley, H.A., Nguyen, T.D., 2015. The effects of glycosaminoglycan degradation on the mechanical behavior of the posterior porcine sclera. *Acta Biomater.* 12, 195–206.
- Norman, R.E., Flanagan, J.G., Sigal, I.A., Rausch, S.M., Tertinegg, I., Ethier, C.R., 2011. Finite element modeling of the human sclera: influence on optic nerve head biomechanics and connections with glaucoma. *Exp. Eye Res.* 93, 4–12.
- Paula, K.Y., McAllister, L.L., Morgan, W.H., Cringle, S.J., Yu, D.-Y., 2017. Interrelationship of arterial supply to human retina, choroid, and optic nerve head using micro perfusion and labeling. *Investig. Ophthalmol. Vis. Sci.* 58, 3565–3574.
- Pavlatos, E., Ma, Y., Clayson, K., Pan, X., Liu, J., 2018. Regional deformation of the optic nerve head and peripapillary sclera during IOP elevation. *Investig. Ophthalmol. Vis. Sci.* 59, 3779–3788.
- Pavlatos, E., Perez, B.C., Morris, H.J., Chen, H., Palko, J.R., Pan, X., Weber, P.A., Hart, R. T., Liu, J., 2016. Three-dimensional strains in human posterior sclera using ultrasound speckle tracking. *J. Biomech. Eng.* 138, 021015.
- Pijanka, J.K., Abass, A., Sorensen, T., Elsheikh, A., Boote, C., 2013. A wide-angle X-ray fibre diffraction method for quantifying collagen orientation across large tissue areas: application to the human eyeball coat. *J. Appl. Crystallogr.* 46, 1481–1489.
- Pijanka, J.K., Coudrillier, B., Ziegler, K., Sorensen, T., MEEK, K.M., Nguyen, T.D., Quigley, H.A., Boote, C., 2012. Quantitative mapping of collagen fiber orientation in non-glaucoma and glaucoma posterior human ScleraeFiber orientation in posterior human sclera. *Investig. Ophthalmol. Vis. Sci.* 53, 5258–5270.
- Pijanka, J.K., Spang, M.T., Sorensen, T., Liu, J., Nguyen, T.D., Quigley, H.A., Boote, C., 2015. Depth-dependent changes in collagen organization in the human peripapillary sclera. *PLoS One* 10, e0118648.
- Quigley, H.A., 1999. Neuronal death in glaucoma. *Prog. Retin. Eye Res.* 18, 39–57.
- Quigley, H.A., 2005. Glaucoma: macrocosm to microcosm the Friedenwald lecture. *Investig. Ophthalmol. Vis. Sci.* 46, 2663–2670.
- Quigley, H.A., Cone, F.E., 2013. Development of diagnostic and treatment strategies for glaucoma through understanding and modification of scleral and lamina cribrosa connective tissue. *Cell Tissue Res.* 353, 231–244.
- Roberts, C.J., Dupps, W.J., Downs, J.C., 2018. *Biomechanics of the Eye*. Kugler Publications.
- Roberts, M.D., Liang, Y., Sigal, I.A., Grimm, J., Reynaud, J., Bellezza, A., Burgoyne, C.F., Downs, J.C., 2010a. Correlation between local stress and strain and lamina cribrosa connective tissue volume fraction in normal monkey eyes. *Investig. Ophthalmol. Vis. Sci.* 51, 295–307.
- Roberts, M.D., Sigal, I.A., Liang, Y., Burgoyne, C.F., Downs, J.C., 2010b. Changes in the biomechanical response of the optic nerve head in early experimental glaucoma. *Investig. Ophthalmol. Vis. Sci.* 51, 5675–5684.
- Sigal, I., Grimm, J., Schuman, J., Kagemann, L., Ishikawa, H., Wollstein, G., 2014a. A method to estimate biomechanics and mechanical properties of optic nerve head tissues from parameters measurable using optical coherence tomography. *IEEE Trans. Med. Imag.* 33, 1381–1389.
- Sigal, I.A., 2009. Interactions between geometry and mechanical properties on the optic nerve head. *Investig. Ophthalmol. Vis. Sci.* 50, 2785–2795.
- Sigal, I.A., 2011. An applet to estimate the IOP-induced stress and strain within the optic nerve head. *Investig. Ophthalmol. Vis. Sci.* 52, 5497–5506.
- Sigal, I.A., Ethier, C.R., 2009. Biomechanics of the optic nerve head. *Exp. Eye Res.* 88, 799–807.
- Sigal, I.A., Flanagan, J.G., Ethier, C.R., 2005a. Factors influencing optic nerve head biomechanics. *Investig. Ophthalmol. Vis. Sci.* 46, 4189–4199.
- Sigal, I.A., Flanagan, J.G., Tertinegg, I., Ethier, C.R., 2004. Finite element modeling of optic nerve head biomechanics. *Investig. Ophthalmol. Vis. Sci.* 45, 4378–4387.
- Sigal, I.A., Flanagan, J.G., Tertinegg, I., Ethier, C.R., 2005b. Reconstruction of human optic nerve heads for finite element modeling. *Technol. Health Care* 13, 313–329.
- Sigal, I.A., Flanagan, J.G., Tertinegg, I., Ethier, C.R., 2007. Predicted extension, compression and shearing of optic nerve head tissues. *Exp. Eye Res.* 85, 312–322.
- Sigal, I.A., Flanagan, J.G., Tertinegg, I., Ethier, C.R., 2009a. Modeling individual-specific human optic nerve head biomechanics. Part I: IOP-induced deformations and influence of geometry. *Biomech. Model. Mechanobiol.* 8, 85–98.
- Sigal, I.A., Flanagan, J.G., Tertinegg, I., Ethier, C.R., 2009b. Modeling individual-specific human optic nerve head biomechanics. Part II: influence of material properties. *Biomech. Model. Mechanobiol.* 8, 99–109.
- Sigal, I.A., Flanagan, J.G., Tertinegg, I., Ethier, C.R., 2010a. 3D morphometry of the human optic nerve head. *Exp. Eye Res.* 90, 70–80.
- Sigal, I.A., Grimm, J.L., 2012. A few good responses: which mechanical effects of IOP on the ONH to study? PCA of ONH biomechanics. *Investig. Ophthalmol. Vis. Sci.* 53, 4270–4278.
- Sigal, I.A., Grimm, J.L., Jan, N.J., Reid, K., Minckler, D.S., Brown, D.J., 2014b. Eye-specific IOP-induced displacements and deformations of human lamina cribrosa. *Invest. Ophthalmol. Vis. Sci.* 55, 1–15.
- Sigal, I.A., Roberts, M.D., Girard, M.J., Burgoyne, C.F., Downs, J.C., 2010b. Biomechanical Changes of the Optic Disc, Ocular Disease. Elsevier, pp. 153–164.
- Sigal, I.A., Yang, H., Roberts, M.D., Burgoyne, C.F., Downs, J.C., 2011a. IOP-induced lamina cribrosa displacement and scleral canal expansion: an analysis of factor interactions using parameterized eye-specific models. *Invest. Ophthalmol. Vis. Sci.* 52, 1896–1907.
- Sigal, I.A., Yang, H., Roberts, M.D., Downs, J.C., 2010c. Morphing methods to parameterize specimen-specific finite element model geometries. *J. Biomech.* 43, 254–262.
- Sigal, I.A., Yang, H., Roberts, M.D., Grimm, J.L., Burgoyne, C.F., Demirel, S., Downs, J.C., 2011b. IOP-induced lamina cribrosa deformation and scleral canal expansion: independent or related? *Investig. Ophthalmol. Vis. Sci.* 52, 9023–9032.

- Voorhees, A., Grimm, J., Bilonick, R., Kagemann, L., Ishikawa, H., Schuman, J., Wollstein, G., Sigal, I., 2016. What is a typical optic nerve head? *Exp. Eye Res.* 149, 40–47.
- Voorhees, A.P., Ho, L.C., Jan, N.-J., Tran, H., van der Merwe, Y., Chan, K., Sigal, I.A., 2017a. Whole-globe biomechanics using high-field MRI. *Exp. Eye Res.* 160, 85–95.
- Voorhees, A.P., Jan, N.-J., Austin, M.E., Flanagan, J.G., Sivak, J.M., Bilonick, R.A., Sigal, I.A., 2017b. Lamina cribrosa pore shape and size as predictors of neural tissue mechanical insult. *Investig. Ophthalmol. Vis. Sci.* 58, 5336–5346.
- Voorhees, A.P., Jan, N.-J., Hua, Y., Yang, B., Sigal, I.A., 2018. Peripapillary sclera architecture revisited: a tangential fiber model and its biomechanical implications. *Acta Biomater.* 79, 113–122.
- Voorhees, A.P., Jan, N.J., Sigal, I.A., 2017c. Effects of collagen microstructure and material properties on the deformation of the neural tissues of the lamina cribrosa. *Acta Biomater.* 58, 278–290.
- Wang, B., Hua, Y., Brazile, B.L., Yang, B., Sigal, I.A., 2020. Collagen fiber interweaving is central to sclera stiffness. *Acta Biomater.* (in press).
- Wang, R., Raykin, J., Gleason Jr., R.L., Ethier, C.R., 2015. Residual deformations in ocular tissues. *J. R. Soc. Interface* 12, 20141101.
- Wang, X., Rumpel, H., Lim, W.E.H., Baskaran, M., Perera, S.A., Nongpiur, M.E., Aung, T., Milea, D., Girard, M.J., 2016. Finite element analysis predicts large optic nerve head strains during horizontal eye movements. *Investig. Ophthalmol. Vis. Sci.* 57, 2452–2462.
- Yan, D., McPheeters, S., Johnson, G., Utzinger, U., Geest, J.P.V., 2011. Microstructural differences in the human posterior sclera as a function of age and race. *Investig. Ophthalmol. Vis. Sci.* 52, 821–829.
- Yang, B., Jan, N.J., Brazile, B., Voorhees, A., Lathrop, K.L., Sigal, I.A., 2018. Polarized light microscopy for 3-dimensional mapping of collagen fiber architecture in ocular tissues. *J. Biophot.* 11, e201700356.
- Yang, H., Downs, J.C., Sigal, I.A., Roberts, M.D., Thompson, H., Burgoyne, C.F., 2009. Deformation of the normal monkey optic nerve head connective tissue after acute IOP elevation within 3-D histomorphometric reconstructions. *Investig. Ophthalmol. Vis. Sci.* 50, 5785–5799.
- Yang, H., Reynaud, J., Lockwood, H., Williams, G., Hardin, C., Reyes, L., Stowell, C., Gardiner, S.K., Burgoyne, C.F., 2017. The connective tissue phenotype of glaucomatous cupping in the monkey eye - clinical and research implications. *Prog. Retin. Eye Res.* 59, 1–52.
- Zhang, L., Albon, J., Jones, H., Gouget, C.L., Ethier, C.R., Goh, J.C., Girard, M.J., 2015. Collagen microstructural factors influencing optic nerve head biomechanics. *Investig. Ophthalmol. Vis. Sci.* 56, 2031–2042.
- Zhou, D., Abass, A., Eliasy, A., Studer, H.P., Movchan, A., Movchan, N., Elsheikh, A., 2019a. Microstructure-based numerical simulation of the mechanical behaviour of ocular tissue. *J. R. Soc. Interface* 16, 20180685.
- Zhou, D., Eliasy, A., Abass, A., Markov, P., Whitford, C., Boote, C., Movchan, A., Movchan, N., Elsheikh, A., 2019b. Analysis of X-ray scattering microstructure data for implementation in numerical simulations of ocular biomechanical behaviour. *PLoS One* 14, e0214770.